coatings

MDPI

Article

Collision of Nanoscale Water Droplets Towards Cylinder Surfaces Under Different Conditions

Siwen Liang [1,2], Ning Ma [2], Chunguang Yang [2], Huihui Hao [2] and Ming Fang [1,*]

[1] School of Artificial Intelligence, Changchun University of Science and Technology, Changchun 130022, China
[2] State Key Laboratory of Special Vehicle Design and Manufacturing Integration Technology, Baotou 014030, China
* Correspondence: fangming@cust.edu.cn

Abstract

Molecular dynamics (MD) simulations are performed to investigate the collision dynamics of two water nanodroplets impinging from opposite directions on a solid fiber. The present work mainly focuses on the effects of some important characteristic parameters, including Weber number, diameter ratio, cylinder diameter, and eccentric distance. For central collision, we observe a total of four outcomes, which are separated droplet bouncing, random detachment, droplet split, and breakup. The maximum spreading factors can be well predicted using βmax~$We2/3Re$-1/3, with βmax~$We1/2Re1/5$ serving as an empirical alternative. The surface wettability cannot affect the scaling law, indicating inertial and viscous forces dominate the spreading process. At a fixed scaling variable, βy, max decreases systematically with increasing diameter ratio due to kinetic-energy and momentum imbalance. Such an imbalance redirects a larger fraction of the incident energy into directional translation rather than lateral spreading. Regime maps further show that, for equal-size collisions, separated droplet bouncing occurs at low Weber numbers, and increasing its value promotes the transition from separated bouncing to random detachment and droplet split. For unequal-size, directional and oblique split replace the random-detachment and droplet-split regimes. In addition, increasing e reduces the effective collision overlap and shifts regime transitions toward higher impact velocity, while droplet-size asymmetry and eccentric collision promote nonuniform film stretching, oblique rupture, and directional separation. These results clarify the coupled roles of inertia, dissipation, thermal fluctuations, and geometric asymmetry in nanoscale droplet transport on curved surfaces.

Keywords: molecular dynamics; two nanodroplet collision; cylindrical surface; maximum spreading factor; droplet-size asymmetry; collision regime transition

Check for updates

Academic Editor: Bohayra Mortazavi

Received: 4 October 2026
Revised: 28 October 2026
Accepted: 28 October 2026
Published: 2 November 2026

Copyright: © 2026 by the authors. Licensee MDPI, Basel, Switzerland. This article is an open access article distributed under the terms and conditions of the Creative Commons Attribution (CC BY) license.

1. Introduction

Collision of water droplets is a ubiquitous phenomenon in both nature and industrial processes, ranging from the formation of clouds and raindrops in the atmosphere to practical engineering applications [1–6]. For this reason, collisions of two droplets have attracted substantial research interest over the past three decades. The dynamic characteristics of droplet collisions have been comprehensively examined using experiments, theoretical frameworks, and numerical simulations [7–13].

A pioneering work in 1997 established a two-dimensional phase diagram, aiming at characterizing collision outcomes under various operating conditions, including Weber number (We), ambient pressure, and type of working liquids [14]. There are a total of

three outcomes from observing photographic images, which are complete coalescence (CO), quick bounce (BO), and reflexive separation (RES) [14]. For the complete coalescence regime, two droplets approach each other, and subsequently a connecting liquid bridge can be formed. The merged droplet then undergoes retraction and dynamical oscillation, and ultimately relaxes into a stable and unified configuration [15]. As the Weber number (*We*) increases, the outcome of droplet collisions changes to a quick bounce, which occurs soon after the droplets come into contact. When *We* exceeds a certain value, unstable coalescence starts, followed by bounce off two collision droplets, namely the RES regime [16]. Here, the Weber number (*We*) is a dimensionless parameter, defined as $We = \rho D_0 {V_0}^2/\gamma$, which represents the ratio of inertial to capillary forces, where ρ, D_0, V_0, and γ denote the density, initial diameter, velocity, and surface tension of colliding droplets, respectively. Numerical simulations were performed to investigate off-center collisions of two droplets [8]. For off-center droplet collision, the dimensionless offset parameter B is used to characterize the off-center distance, which is calculated as $B = X/D_0$. Where X is the distance between the mass centers of the colliding droplets. A new regime is found as progressive increase in B: the merged droplet undergoes continuous rotation, and then it is separated again, forming two repellent components, i.e., rotational separation (ROS) [17]. The mechanisms underlying the mentioned behavioral characteristics have been well revealed in the past. During collision, droplets approach; the air acts as a medium to prevent them from coalescing, which can be gradually compressed into a thin film. Afterward, permanent coalescence (CO) occurs once colliding droplets come into contact, signifying the rupture of the intervening gas film. Once colliding droplets come into contact, inter-droplet flow develops between them, forming a stable liquid bridge and resulting in full coalescence. If the gas cannot be ruptured, colliding droplets will recover their spherical morphology under surface forces and move towards the opposite direction, leading to the BO regime [18,19]. The rotational separation (ROS) regime occurs when rotational motion of the two colliding droplets is triggered under a large offset distance. The rotational separation (ROS) regime emerges for large offset distances, inducing rotational motion of the two colliding droplets [15].

Particularly, ambient pressure exerts a crucial influence on the evolution of droplet collision dynamics, which has attracted substantial attention before. Qian and Law [14] explored droplet collisions of water and hydrocarbons experimentally in air, nitrogen, helium, and ethylene atmospheres. A pressure ranging from 0.6 atm to 12 atm was employed in their experiments. They found that, as gas pressure increases, the BO regime extends significantly until the CO regime cannot be detected, indicating that elevated pressure facilitates the bounce of collision droplets. In addition, physical properties of collision droplets, including viscosity, surface tension, and droplet size, serve as crucial and even dominant factors. Sommerfeld and Kuschel [20] investigated the effect of viscosity on collision dynamics by drawing different phase diagrams over a wide range of *We* and *Oh*. Their work revealed that the triple point (the intersection of BO, SS, and CO regimes) is strongly dependent on the value of *Oh*. Moreover, they deduced a theoretical model to predict the variation of triple points under different viscous conditions, which agrees well with experimental observations. Chen et al. [21] experimentally investigated collisions of nonuniform droplets in systems with either diesel–biodiesel or diesel–water emulsions. In contrast to low-viscosity fluid collisions, a stable liquid bridge readily forms for high-viscosity fluids, which makes SS and RES harder to trigger. The modified VOF method has been adopted to examine collisions of water droplets with various diameter ratios (Δ) [22]. Dynamic monitoring demonstrates that the mass-transfer ratio is irrelevant to the Weber number but varies linearly as collision parameter B increases. Here, the diameter ratio is defined as $\Delta = D_1/D_2$, where D_1 and D_2 denote the diameters of the smaller and larger droplets, respectively. For unequal-size droplet collisions, two distinct splashing dynamics

can be observed via numerical simulations [23]. Large Δ causes finger splashing, whereas small Δ yields flower-shaped splashing due to rim expansion.

For collision droplets at microscopic sizes, it is challenging to capture their interfacial features on a molecular level through experiments or conventional continuum-based numerical simulations [24,25]. By contrast, molecular dynamics (MD) offers a direct route to study nanoscale flows. It resolves the motion of individual atoms via Newton's equations and avoids using complex boundary conditions [26]. Compared with macrosystems, collision of water droplets at the nanoscale produces some intriguing scaling effects, as reported in previous works [27–31]. The main scaling effects encompass enhanced viscous effects, elevated surface-to-volume ratios, and distinct energy dissipation mechanisms. MD simulations have been used to investigate the nanoscale collision of water droplets in a vacuum environment with a wide range of diameters ranging from 10 nm to 100 nm [31]. With enhanced viscous dissipation, the regime of RES dynamics cannot be observed unless the droplet size exceeds 100 nm. By means of MD simulations, Tian et al. [27] studied the nanoscale collision of two unequal-size droplets over a wide range of Weber numbers and off-center distances. They noted a special spreading hysteresis, that is, a dynamic vibration during complete coalescence, across the entire range of Weber numbers [27]. This phenomenon originates from capillary wave propagation inside the merged droplet, which cannot be observed for equal-size collisions.

Recently, water droplet collisions on curved surfaces have gained increasing attention, since surface curvature enables effective tailoring of nanoscale collision dynamics [32,33]. He et al. [32] systematically explored the collision of a single nanodroplet on curved surfaces. The investigation focused on the asymmetrical spreading dynamics induced by curved surfaces and the modification of the contact time (t_c). Here, the contact time, t_c, is defined as the time duration from a nanoscale droplet just touching a solid surface to finally detaching. They divided the regime of the contact time into a stable reducing t regime and a hybrid t regime, according to their MD results. In the stable reducing t regime, the contact time continuously decreases and obeys a law of $t_c \propto \alpha^{-0.226}$. Here, α is a modified Weber number that is defined as $\alpha = We/D^*$, and D^* denotes the diameter ratio of the cylinder to the droplet. For the hybrid t_c regime, as We increases, the contact time first increases owing to a larger wetted area on the curved surface and subsequently decreases toward a limited contact time. There are four distinct impact modes during collision of droplets on curved surfaces, namely spread partially wrapped deposition (SPD), spread completely wrapped deposition (SCD), spread completely wrapped splitting deposition (SCSD), and spread partially wrapped splitting deposition (SPSD) [33]. Therefore, results of collision upon curved surfaces indicate that curved surfaces not only promote atypical behavioral dynamics but also produce some novel outcomes. As mentioned above, the head-on collision is the most common scenario in industrial applications; however, how to employ cylinder surfaces to manipulate the collision of two nanoscale droplets remains unexplored, which may be a good candidate for recovery of polluted aerosols [34,35]. To address this gap, we perform MD simulations to investigate the nanoscale collision of two droplets towards cylinder surfaces under different conditions by observing sequential snapshots, analyzing spreading factor variation, and drawing phase diagrams. These findings yield fundamental insights into the controllable collision dynamics of two nanodroplets over cylindrical surfaces to guide on-demand regulation of their morphological evolution.

2. Simulation Method

In this work, we employ MD simulations using the open-source LAMMPS code to explore the effect of additional cylinder surfaces on collisional water nanodroplets [36,37]. As shown in Figure 1, two nanodroplets and a Pt cylinder surface are placed in the simulated

box, with their centers of mass fixed at (−150, 0, 0), (150, 0, 0), and (0, 0, 0), respectively. Two nanodroplets are identical, consisting of 12,782 water molecules, and the corresponding diameter is 9 nm. The diameter of the cylinder surface is three times smaller than that of the water droplets, with a diameter of D_{cy} = 3 nm. The dimensions of this constructed box are 800 nm in the *x*- direction, 600 nm in the *y*- direction, and 500 nm in the *z*- direction. The collision of water droplets may deform the cylinder surface. To avoid the unexpected deformation, an artificial virtual spring is adopted to immobilize each metal atom at its initial position, thereby enhancing the rigidity of the cylinder surface. In Section 3.3, we change the diameter of the cylinders from 3 nm to 8 nm to further examine the effect of D_{cy} on collision dynamics, and the schematic illustration of changing cylinder-surface diameters is shown in Figure 1.

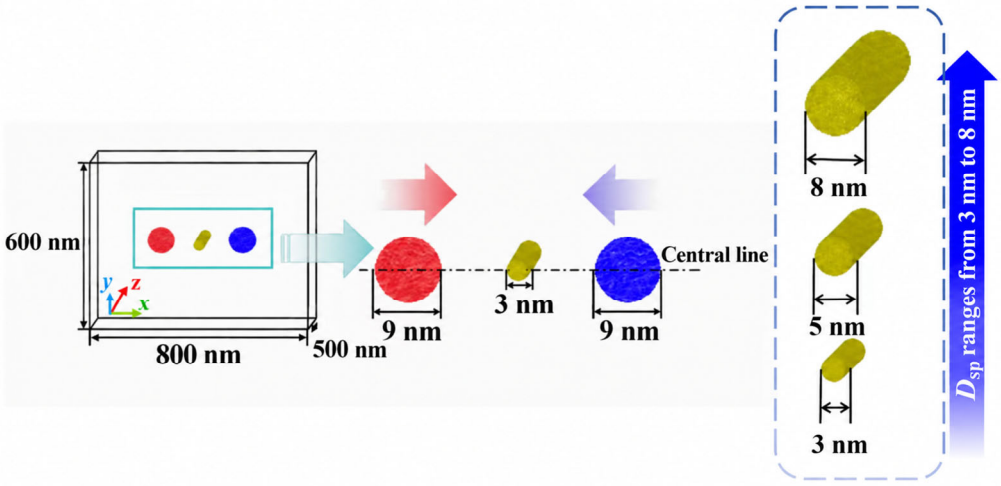


Figure 1. Initial configuration of MD systems, where two identical droplets and Pt cylinder surfaces are placed in a simulated box. The diameters of the two droplets and a cylinder surface are 9 nm and 3 nm, respectively. Here, the diameter of the cylinder surface varies from 3 nm to 8 nm.

The mW water model, a coarse-grained model, is adopted to describe intermolecular interactions between water molecules [38,39]. The mW stands for monatomic water, which adopts the Stillinger–Weber potential with two-body and three-body terms to mimic tetrahedral hydrogen-bonding configurations, without electrostatic interactions. This model is widely adopted as a potential-energy function for exploring nanoscale flow because it not only reduces computational costs (in comparison with the TIP4P and SPC/E models) but also accurately reproduces the physical properties of water. In detail, the mW model gives a density of 0.997 g cm^{-3} and a liquid-vapor surface tension of 66 mN m^{-1}, which agree well with the measured values of bulk water [40]. Nevertheless, this model underestimates viscosity, owing to its omission of hydrogen bond reorientation dynamics. For the mW water model, the intermolecular forces governing both water–Pt and Pt–Pt interactions are described by the Lennard-Jones 12-6 potential [36,37,40], which is expressed as:

$$U_{LJ}(r) = 4\varepsilon\left[\left(\frac{\sigma}{r}\right)^{12} - \left(\frac{\sigma}{r}\right)^{6}\right], r < r_{cut} \quad (1)$$

In this potential function, r signifies the separation distance between the two interacting particles, ε characterizes the strength of the intermolecular attraction (i.e., potential well depth), and σ denotes the distance where the potential energy curve intersects the zero-energy line. In this work, the truncation radius r_{cut} is set to 1 nm, which can reproduce the dynamic behavior of nanodroplets [41,42]. The Lennard-Jones parameters for water–water interactions are set as ε_w = 0.26838 eV and σ_w = 0.23925 nm, whereas those for

Pt–Pt interactions are assigned values of ε_P = 0.69375 eV and σ_P = 0.247 nm. Owing to the absence of a specific potential-energy function for describing solid–liquid interaction, we adopt an alternative approach to modulate this interaction via the parameter $\varepsilon_{w\text{-}Par}$. This parameter is set to 0.0027 eV, and the corresponding contact angle is $\theta_0 = 158^\circ$.

Once the initial configuration of MD systems is established, a 1 ns relaxation run is carried out with a time step of 1 fs to reach the thermodynamic equilibrium state. During the pre-equilibrium stage, the system is operated under the NVT ensemble at a constant temperature of 300 K, achieved by a Nose–Hoover thermostat. In the next step, the ensemble is switched from NVT to NVE, and the system is subjected to a run for a further 1 ns. After that, droplets are assigned a series of different collision velocities to observe the relevant dynamic behaviors. The visualization of atomic trajectories and quantitative analysis of simulation data are accomplished with the help of the Open Visualization Tool (OVITO), a widely used software for molecular dynamics simulation post-processing [43,44]. Moreover, the acronyms in the revised manuscript are listed in Table 1 to facilitate understanding.

Table 1. List of acronyms in the present work.

Abbreviation	Definition
BO	Quick bounce
CO	Complete coalescence
MD	Molecular dynamics
mW	Monatomic water model
NVE	Microcanonical ensemble (constant N, V, and E)
NVT	Canonical ensemble (constant N, V, and T)
OVITO	Open Visualization Tool
RES	Reflexive separation
ROS	Rotational separation
SCD	Spread completely wrapped deposition
SCSD	Spread completely wrapped splitting deposition
SPC/E	Extended simple point charge model
SPD	Spread partially wrapped deposition
SPSD	Spread partially wrapped splitting deposition
SS	Stretching separation
TIP4P	Transferable intermolecular potential with four points
VOF	Volume of fluid method

3. Result and Discussion

3.1. Dynamic Behavior of Collision Droplets of Equal Size

This study investigates the collision of two nanoscale droplets moving in opposite directions toward cylindrical surfaces. In this section, representative free evolution of two identical droplets at different Weber numbers has been observed and studied.

Sequential snapshots of the dynamic behavior of collisional droplets with a progressive increase in *We* are illustrated in Figure 2, and the corresponding variation of the spreading factor in *z*- and *y*- directions (β_z and β_y) of the left droplet is shown in Figure 3. Here, the spreading factor is a dimensionless parameter, normalized by $\beta = D/D_0$. At a low Weber number of *We* = 1.36, two nanodroplets slowly migrate toward the cylindrical surface and eventually come into contact with it, as shown in Figure 2a. The instant of initial contact between the droplets and the cylinder is defined as t = 0 ps. Subsequently, both droplets experience a spreading stage driven by energy conversion between the kinetic energy and the surface energy. However, the fluid is unable to merge into an integrated liquid layer, resulting in only partial coverage of the surface (Figure 2a, t = 10 ps). The variation of the spreading factor at *We* = 1.36 indicates that the spreading stage proceeds asymmetrically, as shown in Figure 3a. After droplet spreading, the extension rate of the

left droplet in the *y*- direction exceeds that in the *z*- direction owing to surface anisotropy, yielding $\beta_{y,max} > \beta_{z,max}$ at the maximum extension state. The observed dynamic evolution of spreading factors is consistent with [32]. At $t > 17$ ps, droplets begin to retract to recover their deformation as stored surface energy returns to kinetic energy (see Figures 2a and 3a). Owing to the absence of the integrated liquid layer, two nanodroplets detach from the cylinder surface and rebound towards the opposite side at $t_c = 55$ ps, namely separated bouncing droplets. Ultimately, bouncing droplets can recover the spherical shape due to surface tension force, with β_y and β_z returning to 1 after 60 ps.

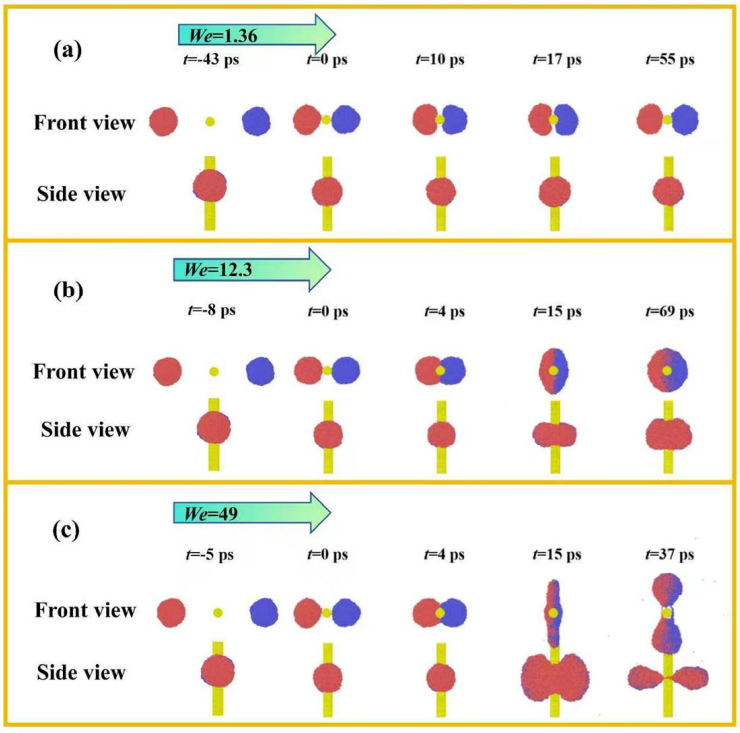


Figure 2. Free evolution of collisional water droplets upon Pt cylinder surface at (**a**) *We* = 1.36, (**b**) *We* = 12.3, and (**c**) *We* = 49.

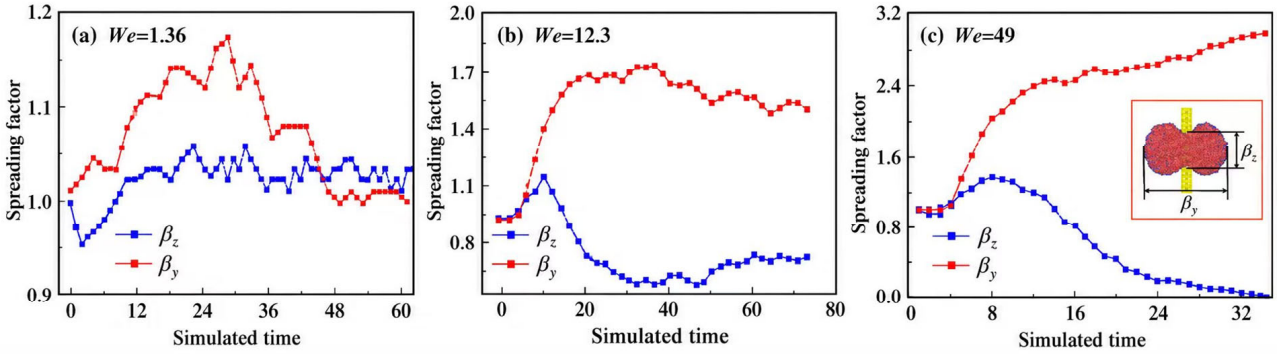


Figure 3. Variation of the spreading factor during droplet collision at various Weber numbers from 1.36 to 49.

As *We* increases to 12.3, the integrated liquid layer covering the cylinder surface can be formed during the collision process, as presented in Figure 2b. First, the spreading factor increases synchronously in both the *z*- and *y*- directions, because the process is dominated by inertial forces (Figure 3b). Distinct dynamic behaviors emerge once the colliding droplets come into contact and form an integrated liquid layer (Figure 2b, 4 ps). The merged droplet exhibits substantial extension along the azimuthal direction, whereas

it retracts along the axial direction. This intriguing phenomenon causes β_y to increase to about 1.72 and β_z to decrease to 0.53, indicating a preferential flow of water molecules in the azimuthal direction. During the retraction stage, the merged droplet stabilizes into an encapsulated state after 69 ps. When the Weber number is increased to 49, splitting of the merged droplet occurs after it experiences the spreading and retracting stage, as shown in Figure 2c. The spreading and subsequent retraction follow a similar trend to that observed at *We* = 12.3, with β_y increasing throughout while β_z rises before decreasing (Figure 3c). The increase in kinetic energy endows water molecules with a higher driving force to flow along the azimuthal direction. As a consequence, β_y decreases continuously until it drops to zero, leading to droplet splitting.

It is well recognized that nanoscale droplets possess an intrinsic energy, i.e., thermal fluctuations, even in the absence of any external stimulus [45,46]. Therefore, the water molecules inside the encapsulating droplet undergo random motion due to thermal fluctuations. As a result, after transient stabilization (Figure 2b, 69 ps), the encapsulating droplet would ultimately depart from the cylinder surface. As shown in Figure 4a, although the input energy is identical, these encapsulating droplets exhibit distinct departing states due to random motion of water molecules, which is a special behavior at the nanoscale. The variation of the average velocity of water molecules inside merged droplets after forming a covering liquid layer is also calculated in Figure 4b–e. The water-molecule velocity shows a high level of dramatic velocity disturbance, and thus, its trajectory is random. The velocity disturbance allows merged droplets to separate from the cylinder surface, leaving an uncertain detachment position.

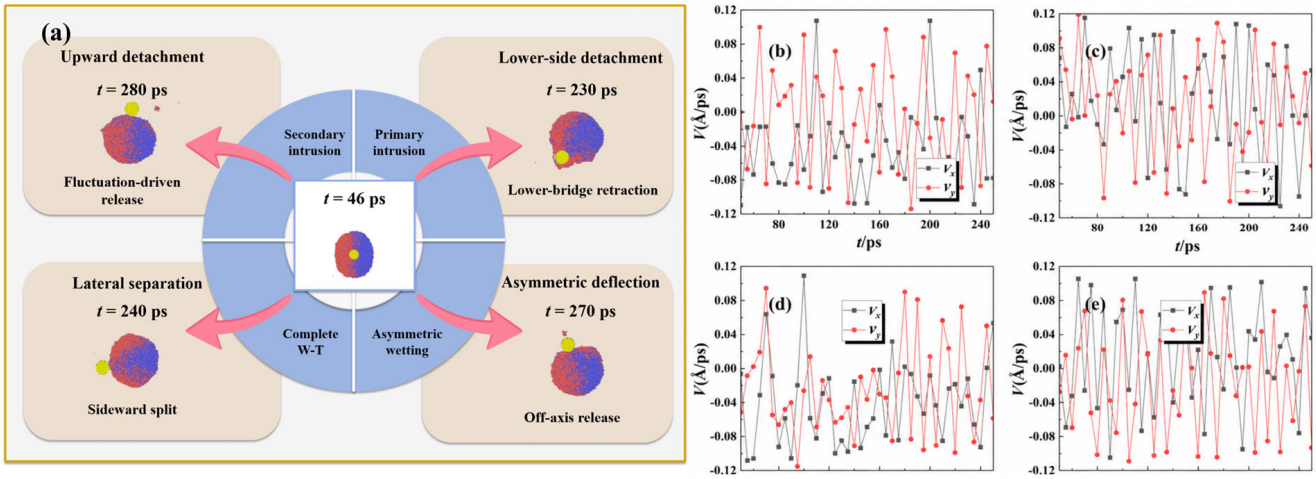


Figure 4. (**a**) Schematic illustration of the different outcomes once a steady state is formed at *We* = 12.3 under various initial pre-equilibrium states. (**b**–**e**) Variation of the average velocity of water molecules inside merged droplets under different initial equilibrium conditions.

At high Weber numbers, the encapsulating droplet undergoes a dramatic spreading process, with irregular hole edges at its periphery, as shown in Figure 5. At 11 ps, the merged droplet evolves into a very thin water film; see the front view in Figure 5. At the nanoscale, the dynamic instability of water films occurs, induced by water-molecule vibration once the thickness of the film reduces below 1 nm [45]. Subsequently, the merged droplet is split into two butterfly-shaped morphologies, with several daughter droplets (breakup).

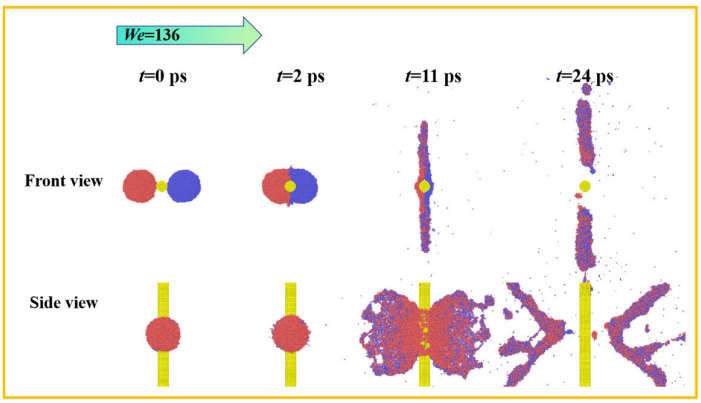


Figure 5. Morphological evolution of collision of two droplets at *We* = 136, exhibiting breakup behavior.

3.2. Variation of Maximum and Minimum Spreading Factor

Previous investigations frequently identified the maximum spreading factor β_{max} as a key parameter governing collision of water droplets, which is highly relevant to many practical applications [26,27]. During nanodroplet impact onto cylinders, the spreading exhibits two distinct extreme spreading states in the azimuthal and axial directions, respectively. Accordingly, we employ $\beta_{y,max}$ and $\beta_{z,min}$ to characterize the distinctive spreading behaviors at different Weber numbers (*We*) and intrinsic wettability (θ_0) before droplet splitting.

A theoretical model for predicting the maximum spreading factor during nanoscale droplet impingement on flat surfaces has been proposed by equating the spreading time, which can be expressed as $\beta_{max} \sim We^{2/3}Re^{-1/3}$. During the encapsulating droplet spreads, the other side of the spreading part should always be regarded as "a flat and rigid surface". Next, we calculate the energy dissipation at progressively increasing Weber numbers, and compare the results with free collision of two droplets, as shown in Figure 6a. The results show that the cylinder surface cannot introduce extra energy dissipation because energy loss at the nanoscale results from bulk dissipation rather than boundary-layer dissipation. Moreover, surface wettability of cylinder surfaces cannot affect the energy dissipation during collision (see Figure 6b). Therefore, we speculate that the maximum spreading factor in the azimuthal direction should also obey the law of $\beta_{y,max} \sim We^{2/3}Re^{-1/3}$. On the other hand, from an energy-balance perspective, the maximum spreading factor, β_{max}, is expected to follow the scaling law of $\beta_{max} \sim We^{1/2}$, derived from the energy balance $\gamma_{lv}D_0^2 \sim E_k V^2$. Nevertheless, for macroscale systems, the impingement induces additional energy dissipation via internal vortex motion. Alternatively, the scaling law of $\beta_{max} \sim We^{1/4}$ is adopted, which agrees well with experimental observations. At the nanoscale, the flow velocity can permeate the whole droplet [47], which can break the mentioned velocity boundary and eliminates the mentioned vortex motion. In addition, the previous investigation demonstrated that energy dissipation for viscous fluid is scaled as $Re^{1/5}$. Therefore, another scaling law of $\beta_{max} \sim We^{1/2}Re^{1/5}$ is proposed to predict $\beta_{y,max}$ for targeted systems. The variation of maximum and minimum spreading factor upon cylinders at different *We* and θ_0 is recorded in Figure 6c,d. Herein, the horizontal axes of Figure 6c,d are $We^{2/3}Re^{-1/3}$ and $We^{1/2}Re^{1/5}$, respectively. The results reveal that the proposed scaling laws $\beta_{y,max} \sim We^{2/3}Re^{-1/3}$ and $\beta_{y,max} \sim We^{1/2}Re^{1/5}$ agree well with MD data across a broad range of Weber numbers. As a consequence, the maximum spreading factor in the *y*- direction can be predicted using two alternative laws, $\beta_{y,max} \sim We^{2/3}Re^{-1/3}$ and $\beta_{y,max} \sim We^{1/2}Re^{1/5}$, with different prefactors. Intriguingly, $\beta_{z,min}$ reduces linearly in Figure 6c,d, yielding $\beta_{z,min} \sim We^{2/3}Re^{-1/3}$ or $We^{1/2}Re^{1/5}$. According to the fitted results in Figure 6a, the maximum spreading factor,

$\beta_{y,\max}$, in the y- direction and the minimum spreading factor in the z- direction, $\beta_{z,\min}$, can be re-expressed as follows:

$$\beta_{y,\,\max} = 1 + 0.35We^{2/3}Re^{-1/3} \tag{2}$$

$$\beta_{z,\,\min} = 1 - 0.15We^{2/3}Re^{-1/3} \tag{3}$$

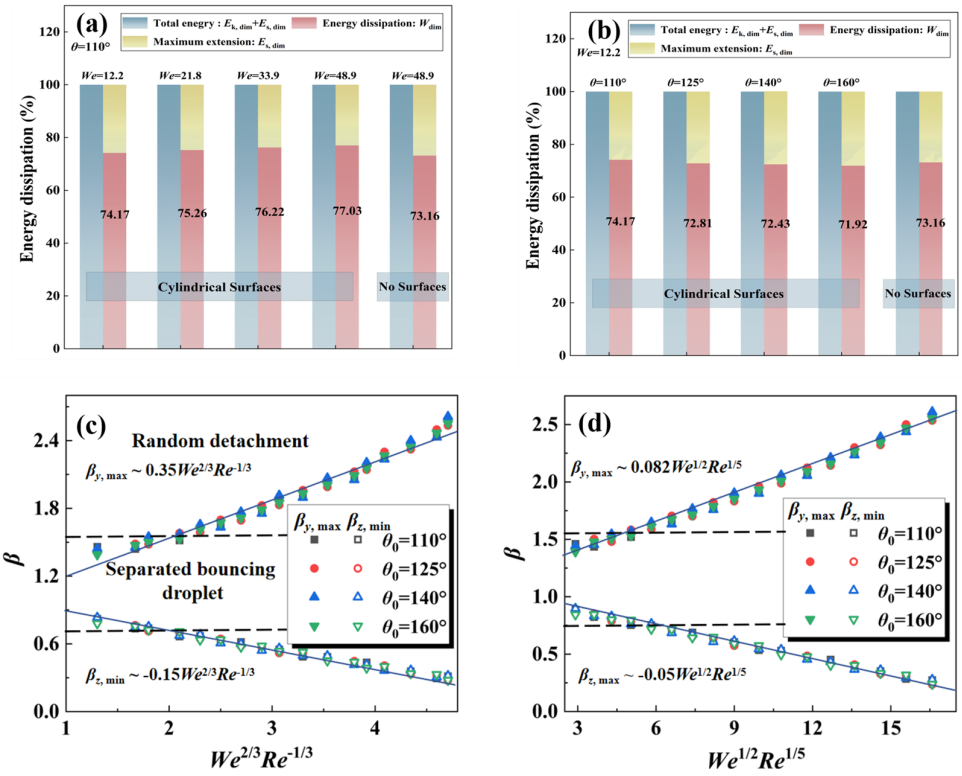


Figure 6. (**a**) Energy dissipation during collision on cylinder surfaces and free collision. (**b**) Effect of surface wettability of cylinders on energy dissipation. (**c**,**d**) Maximum and minimum spreading of $\beta_{y,\max}$ and $\beta_{z,\min}$ versus the law of $\beta_{\max}$~$We^{2/3}Re^{-1/3}$ and $\beta_{\max}$~$We^{1/2}Re^{1/5}$ during collision of two nanodroplets.

Rearranging Equation (3), we derive a new relationship for $\beta_{z,\min}$, which can be expressed as:

$$We^{2/3}Re^{-1/3} = (1 - \beta_{z,\,\min})/0.15 \tag{4}$$

Substituting this expression into Equation (2), the term $We^{2/3}Re^{-1/3}$ can be eliminated, yielding Equation (5).

$$\beta_{y,\,\max} = 1 + (0.35/0.15)(1 - \beta_{z,\,\min}) \approx 3.33 - 2.33\beta_{z,\,\min} \tag{5}$$

Thus, two directional spreading factors exhibit an approximately linear negative correlation. The relationship in Figure 6d can be obtained using the same procedure. The result is directly given by

$$\beta_{y,\,\max} \approx 2.64 - 1.64\beta_{z,\,\min} \tag{6}$$

This confirms that the same linear coupling applies to both scaling forms, although the corresponding coefficients differ. It should be noted that wettability of solid surfaces cannot affect either $\beta_{y,\max}$ or $\beta_{z,\min}$, indicating that the spreading dynamics are governed by inertia rather than capillarity. This observation agrees well with previous investigations for impingement of nanodroplets on flat surfaces. Notably, the dimensionless groups are coupled

through $Oh = We^{1/2}/Re$, giving $We^{2/3}Re^{-1/3} = Oh^{1/3}We^{1/2}$ and $We^{1/2}Re^{1/5} = Oh^{-1/5}We^{3/5}$. At fixed Oh, both are monotonic measures of impact strength. For the specific droplet impact scenario investigated here, we consider $\beta_{y,\max}$~$We^{2/3}Re^{-1/3}$ to be the physically preferred scaling, whereas $\beta_{y,\max}$~$We^{1/2}Re^{1/5}$ is treated as an empirical alternative. This is because the law of $\beta_{y,\max}$~$We^{2/3}Re^{-1/3}$ is consistent with the temporal evolution of inertial, viscous, and capillary forces. Although the law of $\beta_{y,\max}$~$We^{1/2}Re^{1/5}$ can agree well with MD data, it is uncertain to predict the value of $\beta_{y,\max}$ on further increasing droplet scales because of empirical fitting of energy dissipation. To quantify the agreement, the resolvable colored markers in Figure 6 were digitized and fitted separately for the two spreading-factor branches using ordinary least squares with an intercept $\beta_i = aX_i + b$. The values above the original figure are approximate statistics for these new fits; the original image and its plotted curves are retained. Gray markers and unresolved overlapping markers were excluded. The coefficient of determination is defined as follows:

$$R^2 = 1 - \frac{\sum_{i=1}^{n} \left(\beta_i - \hat{\beta}_i\right)^2}{\sum_{i=1}^{n} \left(\beta_i - \overline{\beta}\right)^2} \tag{7}$$

Here, n is the number of digitized points used in the corresponding branch, $\overline{\beta}$ is their mean spreading factor, and $\hat{\beta}_i$ is the fitted value. Each summation runs from $i = 1$ to n. For Figure 6, the estimated R^2 values range from 0.966 to 0.984. These results support approximate linear consistency over the plotted range.

3.3. Collision of Nanodroplets Under Different Conditions

Particularly, the diameter ratio, Δ, is a vital characteristic parameter governing the collision dynamics. To elucidate the coupled effects of droplet-size asymmetry and inertia force, the dynamics of dissimilar-sized nanodroplets at $\Delta = 1.8$ are selected as representative evolution, as shown in Figure 7. Noticeably, In each case, the two droplets are assigned an identical Weber number ranging from 1.36 and 49 to 87. Here, V_l and V_r denote the initial x- direction impact velocities of the left and right droplets, respectively, while D_l and D_r denote their corresponding initial diameters. According to the definition of the Weber number, we have $D_\mathrm{l}{V_\mathrm{l}}^2 = D_\mathrm{r}{V_\mathrm{r}}^2$ due to the same We values, and thus, the velocity ratio of right to left droplets can be calculated as $V_\mathrm{r}/V_\mathrm{l} = (D_\mathrm{l}/D_\mathrm{r})^{1/2}$. Since the right droplet has a smaller diameter in the present configuration ($D_\mathrm{r} < D_\mathrm{l}$), it follows that $V_\mathrm{r} > V_\mathrm{l}$. Under the same Weber number condition, the right droplet impacts the cylinder at a higher absolute velocity. At $We = 1.36$, the inertial effect remains insufficient to form a continuous liquid film around the cylinder, as shown in Figure 7a. The droplets deform as kinetic energy is converted to surface energy and then retract, resulting in separated droplet bouncing like $\Delta = 1$. Variation of velocity in Figure 7d shows that both V_r and V_l decrease and subsequently increase during the separated-droplet-bouncing stage. Moreover, the cylinder acquires only a small positive x- direction velocity and moves towards the left side due to the asymmetric momentum (see Figure 7a,d). When We increases to 49, the enhanced inertial effect promotes more extensive spreading and enables the two droplets to form the integrated liquid film wrapping the cylinder, as shown in Figure 7b. After that, the merged droplet detaches from the cylinder and moves towards the left side, with pronounced motion of the surface, i.e., directional motion of the merged droplet (see Figure 7b,e). As can be seen in Figure 7e, V_cyl is markedly lower than V_mer, indicating that only part of the incident momentum is transferred to the cylinder. On further increasing We to 87, the droplet deformation and interfacial stretching become more intense, and the merged droplet shows a tendency toward local rupture. Meanwhile, momentum transfer to the

cylinder is substantially enhanced with a further increase in velocity. Consequently, V_{cyl} progressively approaches V_{mer} and becomes approximately equal to it at the later stage (Figure 7c,f), indicating nearly synchronous translational motion of the cylinder and the merged droplet. Overall, for collision with unequal-size droplets, increasing *We* strengthens the dominance of inertia effect, resulting in progressively stronger spreading, deformation, coalescence, directional migration, and interfacial instability.

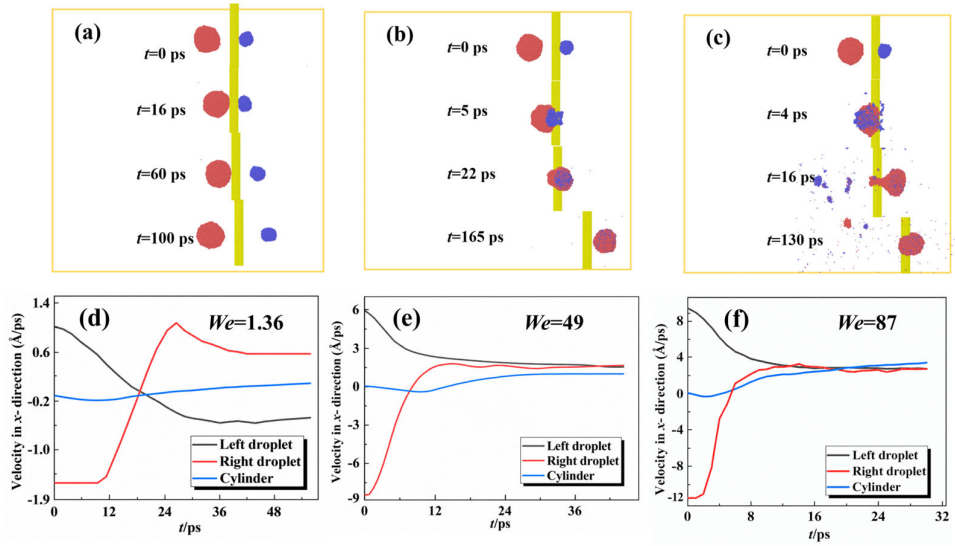


Figure 7. Dynamic evolution of colliding droplets with Δ = 1.8 at (**a**) *We* = 1.36, (**b**) *We* = 49, and (**c**) *We* = 87. The velocity variation in the *x*- direction corresponds to the collision at (**d**) *We* = 1.36, (**e**) *We* = 49, and (**f**) *We* = 87.

Figure 8 extends the scaling analysis in Figure 5 to explore the maximum and minimum spreading factor over droplet collision. For all these cases, $\beta_{y,max}$ increases approximately linearly with $We^{2/3}Re^{-1/3}$ [Figure 8a–c] and $We^{1/2}Re^{1/5}$ [Figure 8d–f], whereas $\beta_{z,min}$ exhibits the reverse trend, decreasing accordingly. This observation confirms that the scaling relations remain applicable for varying Δ, indicating that no extra energy dissipation is introduced. For variation $\beta_{y,max}$, Figure 7a,d show the steepest fitted slopes at Δ = 1, indicating that equal-size collision allows a larger fraction of the kinetic energy to contribute to lateral spreading. When Δ increases to 1.5 Figure 8b,e, the fitted slopes decrease, showing that the growth rate of $\beta_{y,max}$ with increasing inertial contribution is weakened. At Δ = 1.8, Figure 8c,f, the slopes become the smallest among the three cases. This is because unequal-size collisions induce a tendency of directional motion, which is unfavorable for lateral spreading. In contrast, the fitted slopes of $\beta_{z,min}$ remain nearly unchanged as Δ increases. This weak dependence is mainly attributed to the smaller droplet, which contributes relatively little to deformation in the *z*- direction. Increasing Δ therefore primarily redistributes the incident energy and momentum toward directional translation and *y*-direction spreading, while only weakly modifying axial contraction. Consequently, $\beta_{z,min}$ is less sensitive to droplet-size asymmetry, and its fitted slope shows only minor variation among the three diameter ratios. The limited scatter among different θ_0 values further indicates that inertia remains the dominant factor, whereas wettability has only a weak influence on the spreading magnitude. Using the same digitization and fitting procedure, the estimated R^2 values in Figure 8 range from 0.966 to 0.986. Across Figures 6 and 8, $R^2 \approx$ 0.966–0.986. The results support approximate linear consistency of the characteristic spreading factors with the selected scaling variables within the investigated range. Because these estimates use only resolvable digitized markers, they do not establish a unique scaling law or the absence of additional dissipation.

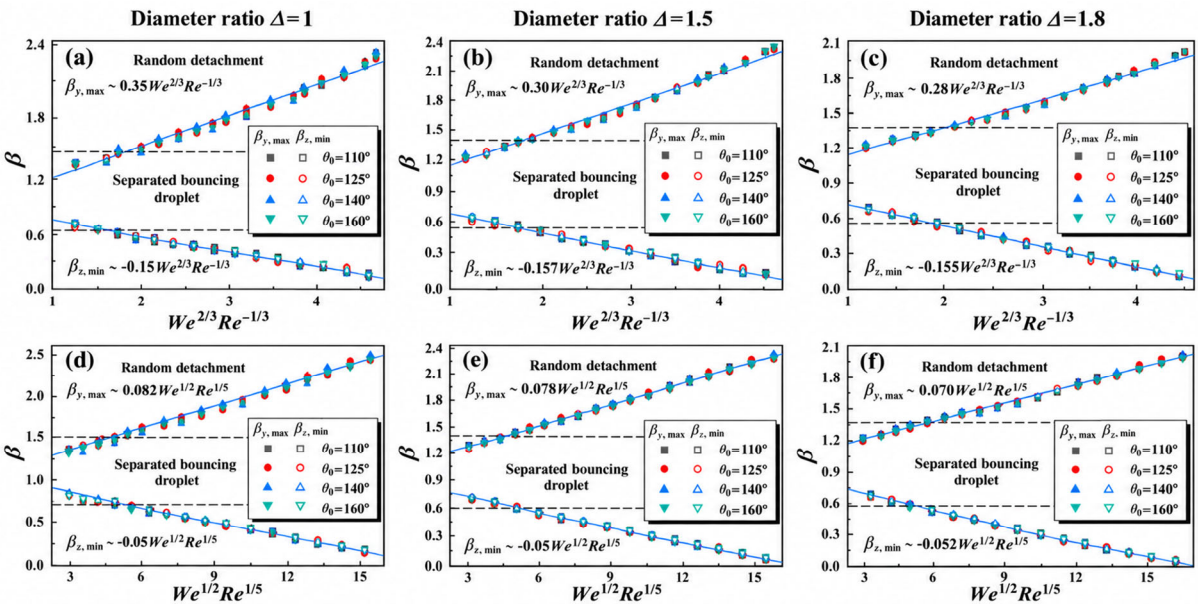


Figure 8. Maximum and minimum spreading factors $\beta_{y,max}$ and $\beta_{z,min}$ versus $We^{2/3}Re^{-1/3}$ (**a**–**c**) and $We^{1/2}Re^{1/5}$ (**d**–**f**) for Δ = 1, 1.5, and 1.8 from left to right. Symbols denote MD results at different θ_0; the upper and lower branches correspond to $\beta_{y,max}$ and $\beta_{z,min}$, respectively, while solid and dashed lines indicate linear fits and regime boundaries, respectively.

Figure 9 summarizes the phase diagrams for collisions of water droplets with different Δ ranging from 1 to 1.5 to 1.8 upon a cylinder surface with different diameters from D_{cy} = 30 to 80 Å to obtain overall insights into the effect of Δ and D_{cy} on the head-on collision regime. To validate the accuracy of the phase diagram, four replicate simulations were performed at each phase boundary. These repeated runs help confirm the regime transition and quantify boundary uncertainty. For Δ = 1 (Figure 9a), separated droplet bouncing occupies the low-*We* region. Increasing *We* promotes coalescence and random detachment, followed by droplet splitting at moderate *We* and breakup at the highest *We* range. The bouncing-to-detachment boundary moves from approximately *We* = 25 at D_{cy} = 30 Å to *We* = 70 at D_{cy} = 80 Å, whereas the onset of splitting remains near *We* = 80. Thus, increasing D_{cy} mainly narrows the random-detachment region. This trend is because the spreading interfaces need to traverse around a larger cylinder to promote separated bouncing droplets as D_{cy} increases, as shown in Figure 9d. If spreading is insufficient, the droplets retract before forming a continuous liquid bridge and rebound separately. For Δ = 1.5 and 1.8 (Figure 9b,c), directional motion and oblique split replace the random-detachment and droplet-split regimes observed for equal-sized droplets. Directional motion is concentrated at smaller D_{cy} and intermediate *We*; at larger D_{cy}, bouncing gives way directly to oblique split within the sampled conditions. This trend indicates that stronger droplet-size asymmetry reduces the stability of the coalesced state. At a fixed Weber number, the asymmetry in both momentum and kinetic-energy input therefore becomes more pronounced as Δ gradually increases. As a consequence, a larger fraction of the incident energy is redirected to directional transport and nonuniform interfacial deformation, promoting oblique rupture (see Figure 9e) and advancing the onset of breakup.

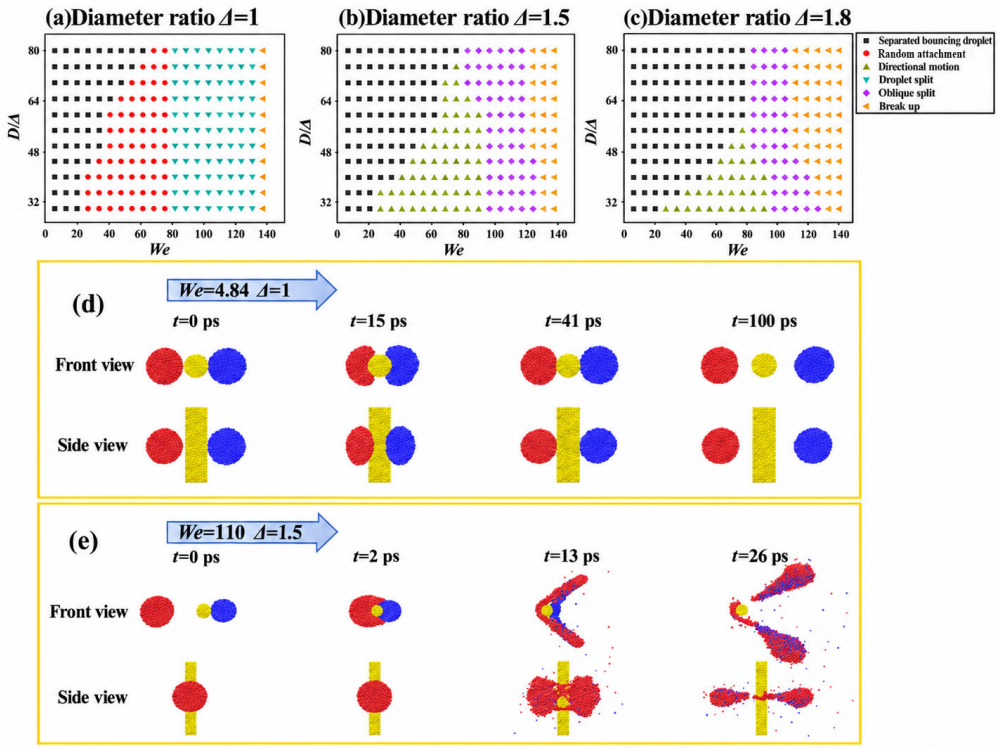


Figure 9. Phase diagrams of possible outcomes under different diameter ratios: (**a**) Δ = 1, (**b**) Δ = 1.5, and (**c**) Δ = 1.8. (**d**,**e**) Morphological evolution of oblique splitting for unequal-sized colliding droplets at *We* = 110 and Δ = 1.5.

As shown in Figure 10, the phase diagrams summarize the possible collision outcomes over a wide range of Weber numbers (*We*) and eccentric distances (*e*). Here, *e* denotes the eccentric distance of the collisional configuration. For equal-sized droplets (Δ = 1), low-*We* collisions are mainly characterized by bouncing behaviors, including separated bouncing droplets and oblique bouncing. As shown in Figure 10d, oblique bouncing typically occurs in the low-*We* regime, where the inertial effect is insufficient to maintain a stable liquid bridge around the cylindrical surface. Ultimately, the merged liquid mass separates into two droplets and rebounds away from the cylinder without forming a stable coalesced body. Under these conditions, the supplied kinetic energy is insufficient to sustain a stable liquid film around the cylinder, thereby bouncing after limited spreading. When *e* increases, the overlap between the two droplets is reduced, and the interaction with the cylindrical surface becomes weaker, which makes the rebound process more irregular and favors oblique bouncing. With increasing *We*, enhanced inertia promotes more pronounced spreading and transient interaction around the cylinder, giving rise to rebound attachment or directional motion. A further increase in *We* results in a thinner and more strongly stretched liquid film, and the collision outcome gradually changes to oblique split. At the highest *We*, severe deformation and interfacial instability finally lead to breakup. For unequal-sized droplets (Δ = 1.5 and 1.8), the regime distribution becomes increasingly asymmetric. Since the kinetic-energy ratio of the two droplets follows $E_l/E_r = \Delta^2$, increasing Δ strengthens the momentum imbalance on the two sides of the cylinder. Consequently, the bouncing directional motion regimes shrink, whereas the oblique split regime expands over a broader intermediate-to-high *We* range. Meanwhile, increasing *e* shifts most transition boundaries toward higher *We* because the enlarged eccentric distance reduces the effective collision overlap and makes complete wrapping around the cylinder more difficult. Nevertheless, once sufficient inertia is supplied, the combined effects of eccentric impact and droplet-size mismatch intensify the nonuniform stretching of the liquid film, thereby facilitating oblique

rupture and eventual breakup. Overall, *We* primarily controls the degree of deformation and film stretching, whereas *e* and Δ together govern the collision asymmetry and the transition among oblique bouncing, separated bouncing droplet, rebound attachment, directional motion, oblique split, and breakup.

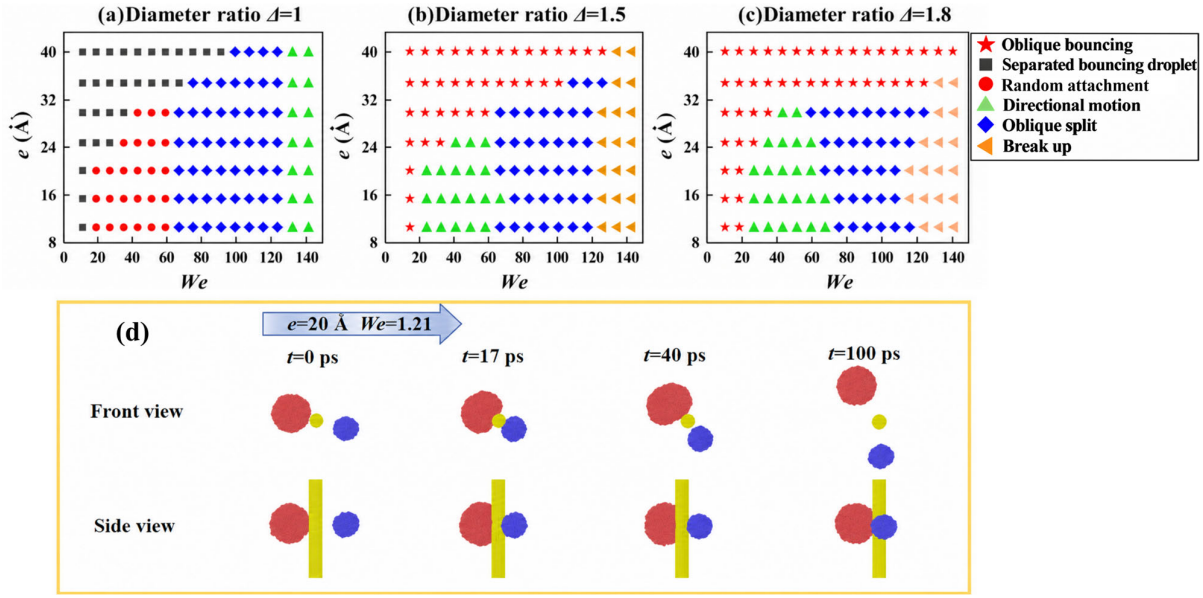


Figure 10. Phase diagrams of two nanodroplet collision regimes as functions of *We* and *e* at different diameter ratios: (**a**) Δ = 1, (**b**) Δ = 1.5, and (**c**) Δ = 1.8. (**d**) Morphological evolution of random separated bouncing.

4. Conclusions

In this study, molecular dynamics simulations were performed to systematically investigate the collision dynamics of two water nanodroplets interacting with a Pt cylindrical surface. For equal-sized droplets, four representative collision outcomes were identified, including separated droplet bouncing, random detachment, droplet split, and breakup. At low *We*, the inertial effect is insufficient to sustain a continuous liquid film around the cylinder, and the droplets retract and rebound separately. As *We* increases, enhanced inertia promotes spreading and coalescence around the cylindrical surface, followed by random detachment owing to nanoscale thermal fluctuations. At higher *We*, stronger interfacial stretching produces a thinner liquid film and eventually induces splitting and breakup through interfacial instability.

The spreading behavior can be quantitatively characterized by the maximum spreading factor in the azimuthal direction, $\beta_{y,\max}$, and the minimum spreading factor in the axial direction, $\beta_{z,\min}$. The MD results demonstrate that both characteristic spreading factors can be described by the scaling variables $We^{2/3}Re^{-1/3}$ and $We^{1/2}Re^{1/5}$, confirming that inertia and viscous dissipation dominate the spreading process. For unequal-sized droplets, the scaling relations remain applicable; however, the fitted slope of $\beta_{y,\max}$ decreases progressively with increasing Δ, while that of $\beta_{z,\min}$ remains nearly unchanged. The weak dependence of $\beta_{z,\min}$ on Δ arises because the smaller droplet contributes relatively little to the axial deformation. Increasing droplet-size asymmetry therefore mainly redistributes the incident energy toward directional translation and azimuthal spreading, while only weakly modifying axial contraction. Under the same Weber number condition, droplet-size asymmetry further introduces distinct energy and momentum transfer between the two droplets. Because $D_l V_l^2 = D_r V_r^2$, the smaller droplet possesses a higher impact velocity, and thus the corresponding translational kinetic-energy ratio satisfies $E_l/E_r = \Delta^2$. Consequently,

increasing Δ enhances the imbalance in the incident energy and momentum, redirecting a larger fraction of the available energy toward directional motion of the merged droplet and cylinder and reducing the fraction available for lateral spreading.

The regime maps further demonstrate the coupled influences of We, D_{cy}, Δ, and e on collision outcomes. Increasing D_{cy} increases the circumferential distance required for the spreading interfaces to merge and consequently narrows the random-detachment region. Increasing Δ suppresses symmetric collision outcomes and promotes directional motion, oblique splitting, and breakup owing to the enhanced asymmetry of energy and momentum transfer. Meanwhile, increasing e reduces the effective collision overlap, weakens the interaction between the droplets and the cylindrical surface, and shifts the regime transitions toward higher We. At sufficiently high We, the combined effects of droplet-size asymmetry and eccentric collision intensify nonuniform film stretching, leading to oblique split. These findings clarify the coupled roles of inertia, viscous dissipation, thermal fluctuations, and geometric asymmetry in two nanodroplet collisions on curved surfaces, which provides a physical basis for regulating nanoscale liquid transport, directional migration, and separation.

Supplementary Materials: The following supporting information can be downloaded at: https://www.mdpi.com/article/10.3390/coatings16111302/s1. All data files.

Author Contributions: Conceptualization, S.L. and N.M.; methodology, S.L.; software, N.M. and H.H.; validation, S.L., C.Y. and H.H.; formal analysis, N.M. and H.H.; investigation, S.L. and H.H.; resources, C.Y.; data curation, S.L.; writing—original draft preparation, S.L.; writing—review and editing, M.F.; visualization, M.F.; supervision, M.F.; project administration, C.Y.; funding acquisition, M.F. All authors have read and agreed to the published version of the manuscript.

Funding: This research received no specific grant from any funding agency in the public, commercial, or not-for-profit sectors. There was no external financial support provided for the conduct of this study or the preparation of the manuscript.

Institutional Review Board Statement: Not applicable.

Informed Consent Statement: Not applicable.

Data Availability Statement: The original contributions presented in the study are included in the Supplementary Materials, further inquiries can be directed to the corresponding author.

Conflicts of Interest: The authors declare no conflicts of interest.

References

1. Adam, J.R.; Lindblad, N.R.; Hendricks, C.D. The collision, coalescence, and disruption of water droplets. *J. Appl. Phys.* **1968**, *39*, 5173–5180. [CrossRef]
2. Pan, K.L.; Chou, P.C.; Tseng, Y.J. Binary droplet collision at high Weber number. *Phys. Rev. E* **2009**, *80*, 036301. [CrossRef]
3. Nikolopoulos, N.; Theodorakakos, A.; Bergeles, G. Off-centre binary collision of droplets: A numerical investigation. *Int. J. Heat Mass Transf.* **2009**, *52*, 4160–4174. [CrossRef]
4. Focke, C.; Kuschel, M.; Sommerfeld, M.; Bothe, D. Collision between high and low viscosity droplets: Direct Numerical Simulations and experiments. *Int. J. Multiph. Flow* **2013**, *56*, 81–92. [CrossRef]
5. Orme, M. Experiments on droplet collisions, bounce, coalescence and disruption. *Prog. Energy Combust. Sci.* **1997**, *23*, 65–79. [CrossRef]
6. Tkachenko, P.P.; Shlegel, N.E.; Strizhak, P.A. Collisions of water droplets in the high-temperature air. *Int. J. Heat Mass Transf.* **2021**, *170*, 121011. [CrossRef]
7. Kuan, C.K.; Pan, K.L.; Shyy, W. Study on high-Weber-number droplet collision by a parallel, adaptive interface-tracking method. *J. Fluid Mech.* **2014**, *759*, 104–133. [CrossRef]
8. Lycett-Brown, D.; Luo, K.H.; Liu, R.; Lv, P. Binary droplet collision simulations by a multiphase cascaded lattice Boltzmann method. *Phys. Fluids* **2014**, *26*, 023303. [CrossRef]
9. Zhang, Y.R.; Luo, K.H. Regimes of head-on collisions of equal-sized binary droplets. *Langmuir* **2019**, *35*, 8896–8902. [CrossRef]

10. Inamuro, T.; Tajima, S.; Ogino, F. Lattice Boltzmann simulation of droplet collision dynamics. *Int. J. Heat Mass Transf.* **2004**, *47*, 4649–4657. [CrossRef]
11. Sun, K.; Zhang, P.; Jia, M.; Wang, T. Collision-induced jet-like mixing for droplets of unequal-sizes. *Int. J. Heat Mass Transf.* **2018**, *120*, 218–227. [CrossRef]
12. Wang, F.C.; Feng, J.T.; Zhao, Y.P. The head-on colliding process of binary liquid droplets at low velocity: High-speed photography experiments and modeling. *J. Colloid Interface Sci.* **2008**, *326*, 196–200. [CrossRef]
13. Ray, S.; Han, Y.; Cheng, S. Pinch-off dynamics in unequal-size droplets head-on collision on a wetting surface: Experiments and direct numerical simulations. *Phys. Fluids* **2023**, *35*, 122105. [CrossRef]
14. Qian, J.; Law, C.K. Regimes of coalescence and separation in droplet collision. *J. Fluid Mech.* **1997**, *331*, 59–80. [CrossRef]
15. Pan, K.L.; Huang, K.L.; Hsieh, W.T.; Lu, C.R. Rotational separation after temporary coalescence in binary droplet collisions. *Phys. Rev. Fluids* **2019**, *4*, 123602. [CrossRef]
16. Pan, K.L.; Law, C.K.; Zhou, B. Experimental and mechanistic description of merging and bouncing in head-on binary droplet collision. *J. Appl. Phys.* **2008**, *103*, 064901. [CrossRef]
17. Chen, X.; Yang, V. Direct numerical simulation of multiscale flow physics of binary droplet collision. *Phys. Fluids* **2020**, *32*, 062103. [CrossRef]
18. Willis, K.; Orme, M. Binary droplet collisions in a vacuum environment: An experimental investigation of the role of viscosity. *Exp. Fluids* **2003**, *34*, 28–41. [CrossRef]
19. Sommerfeld, M.; Kuschel, M. Modelling droplet collision outcomes for different substances and viscosities. *Exp. Fluids* **2016**, *57*, 187. [CrossRef]
20. Chen, R.H.; Wang, W.C.; Chen, Y.W. Like-drop collisions of biodiesel and emulsion diesel. *Eur. J. Mech.-B/Fluids* **2016**, *60*, 62–69. [CrossRef]
21. Chen, X.; Ma, D.; Yang, V. Collision outcome and mass transfer of unequal-sized droplet collision. In Proceedings of the 50th AIAA Aerospace Sciences Meeting Including the New Horizons Forum and Aerospace Exposition, Nashville, TN, USA, 9–12 January 2012.
22. Cong, H.; Qian, L.; Wang, Y.; Lin, J. Numerical simulation of the collision behaviors of binary unequal-sized droplets at high Weber number. *Phys. Fluids* **2020**, *32*, 103307. [CrossRef]
23. Taheri, M.H.; Mohammadpourfard, M.; Sadaghiani, A.; Kosar, A. Wettability alterations and magnetic field effects on the nucleation of magnetic nanofluids: A molecular dynamics simulation. *J. Mol. Liq.* **2018**, *260*, 209–220. [CrossRef]
24. Taherian, F.; Marcon, V.; Bonaccurso, E.; van der Vegt, N.F.A. Vortex formation in coalescence of droplets with a reservoir using molecular dynamics simulations. *J. Colloid Interface Sci.* **2016**, *479*, 189–198. [CrossRef]
25. Li, Y.X.; Xu, J.L.; Li, D.Q. Molecular dynamics simulation of nanoscale liquid flows. *Microfluid. Nanofluidics* **2010**, *9*, 1011–1031. [CrossRef]
26. Tian, Y.Y.; Ma, M.Y.; Chen, Z.Y.; Cui, K.; Du, J.F.; Yu, C.; Wang, S.L.; He, X. Collision of nanoscale water droplets: A molecular dynamics study. *Phys. Fluids* **2025**, *37*, 012025. [CrossRef]
27. He, X.; Cui, K.; Dong, W.H.; Zhang, X.J.; Zhou, Z.F.; Wang, S.L. Investigation of dynamic characteristics of impacting nanodroplets on solid surfaces decorated with a stepped texture. *Colloids Surf. A Physicochem. Eng. Asp.* **2023**, *670*, 131581. [CrossRef]
28. He, X.; Dong, W.H.; Cui, K.; Fan, J.S.; Wang, T.Y.; Yu, C.; Wang, S.L. Contact time of impacting nanodroplets on cylinder surfaces. *J. Mol. Liq.* **2024**, *410*, 125459. [CrossRef]
29. Zhang, A.P.; Cui, K.; Tian, Y.Y.; Wang, T.Y.; He, X. Dynamic characteristics of impacting binary nanodroplets on solid surfaces: From hydrophobic to superhydrophobic. *J. Mol. Liq.* **2023**, *389*, 122873. [CrossRef]
30. Zhang, Y.R.; Zhao, Z.J.; Luo, K.H.; Shi, B. Size effects on dynamics of nanodroplets in binary head-on collisions. *J. Mol. Liq.* **2021**, *341*, 117383. [CrossRef]
31. Liu, X.C.; Liu, L.S.; Li, R.J.; Xie, J. Morphological evolution of nano-droplets impinging on cylindrical wall: A molecular dynamics study. *J. Mol. Liq.* **2024**, *403*, 124900. [CrossRef]
32. Thompson, A.P.; Aktulga, H.M.; Berger, R.; Bolintineanu, D.S.; Brown, W.M.; Crozier, P.S.; In 't Veld, P.J.; Kohlmeyer, A.; Moore, S.G.; Nguyen, T.D.; et al. LAMMPS—A flexible simulation tool for particle-based materials modeling at the atomic, meso, and continuum scales. *Comput. Phys. Commun.* **2022**, *271*, 108171. [CrossRef]
33. Plimpton, S. Fast parallel algorithms for short-range molecular dynamics. *J. Comput. Phys.* **1995**, *117*, 1–19. [CrossRef]
34. Wang, C.; Wu, X.; Zhang, H.; Hao, P.; He, F.; Zhang, X. A many-body dissipative particle dynamics study of eccentric droplets impacting inclined fiber. *Phys. Fluids* **2021**, *33*, 042001. [CrossRef]
35. Piroird, K.; Clanet, C.; Lorenceau, E.; Quere, D. Drops impacting inclined fibers. *J. Colloid Interface Sci.* **2009**, *334*, 70. [CrossRef]
36. Molinero, V.; Moore, E.B. Water modeled as an intermediate element between carbon and silicon. *J. Phys. Chem. B* **2009**, *113*, 4008–4016. [CrossRef]
37. Jacobson, L.C.; Kirby, R.M.; Molinero, V. How short is too short for the interactions of a water potential? Exploring the parameter space of a coarse-grained water model using uncertainty quantification. *J. Phys. Chem. B* **2014**, *118*, 8190–8202. [CrossRef]

38. He, X.; Wang, S.L.; Yang, Y.R.; Wang, X.D.; Chen, J.Q. Electro-coalescence of two charged droplets under pulsed direct current electric fields with various waveforms: A molecular dynamics study. *J. Mol. Liq.* **2020**, *312*, 113429. [CrossRef]
39. Chen, Q.C.; Ma, J.; Zhang, Y.J.; Wu, C.L.; Xu, J.L. Effects of temperature and ionic concentration on nanodroplet electrocoalescence. *Langmuir* **2019**, *35*, 750–759. [CrossRef]
40. He, X.; Wang, Y.F.; Cui, K.; Tian, Y.Y.; Yu, C.; Wang, X.D. Controllable wetting characteristics of hierarchically structured surfaces. *J. Colloid Interface Sci.* **2026**, *702*, 138961. [CrossRef]
41. Cai, Z.H.; Wang, Y.F.; He-Liu, R.X.; Zhu, K.Q.; Zhang, B.X.; Zheng, S.F.; Huang, C.L.; Yang, Y.R.; Wang, X.D. The maximum spreading factor and restitution coefficient for impacts of nanodroplets on spheres. *Phys. Fluids* **2026**, *38*, 032106. [CrossRef]
42. Stukowski, A. Visualization and analysis of atomistic simulation data with OVITO—The Open Visualization Tool. *Model. Simul. Mater. Sci. Eng.* **2010**, *18*, 015012. [CrossRef]
43. Gopan, N.; Sathian, S.P. The role of thermal fluctuations on the formation and stability of nano-scale drops. *Colloids Surf. A Physicochem. Eng. Asp.* **2013**, *432*, 19–28. [CrossRef]
44. Choi, Y.S.; Kim, S.J.; Kim, M.-U. Molecular dynamics of unstable motions and capillary instability in liquid nanojets. *Phys. Rev. E* **2006**, *73*, 016309. [CrossRef]
45. Li, B.X.; Li, X.H.; Chen, M. Spreading and breakup of nanodroplet impinging on surface. *Phys. Fluids* **2017**, *29*, 012003. [CrossRef]
46. Du, J.Y.; Wang, X.; Li, Y.Z.; Min, Q.; Wu, X.X. Analytical consideration for the maximum spreading factor of liquid droplet impact on a smooth solid surface. *Langmuir* **2021**, *37*, 7582–7590. [CrossRef]
47. Clanet, C.; Béguin, C.; Richard, D.; Quéré, D. Maximal deformation of an impacting drop. *J. Fluid Mech.* **2004**, *517*, 199–208. [CrossRef]

Disclaimer/Publisher's Note: The statements, opinions and data contained in all publications are solely those of the individual author(s) and contributor(s) and not of MDPI and/or the editor(s). MDPI and/or the editor(s) disclaim responsibility for any injury to people or property resulting from any ideas, methods, instructions or products referred to in the content.